Supporting Information

From Wilhelm *et al.*, 2022 – Susceptibility of new soil organic carbon to mineralization during dry-wet cycling in soils from contrasting ends of a precipitation gradient.

Quantification of total metals in bulk soil

Total metals were measured by microwave digestion with HNO_3/HCl/HF using an Ethos Milestone Microwave Digester (Milestone Scientific, Inc., Livingston, NJ). Dried samples (105 °C for 24 h) were pulverized with an agate shatter box. Samples were then combusted in a muffle furnace at 500 °C for 4 h followed by 950ºC for 30 min to convert Fe^{2+} to Fe^{3+} and remove organic carbon and structural water. Following ignition, samples were digested in a 3:2:0.25 solution of HNO_3:HCl:HF at 200 °C for 40 min. Samples were cooled to 25 °C and boric acid (4 wt %) was added. This solution was then heated to 150 ºC for 20 min to neutralize excess HF, while retaining dissolved SiO_2. The USGS standard BHVO-2 was used as a reference material and procedural blanks were measured every 10 samples. Following digestion, samples were immediately diluted 10,000-times for analysis using a SpectroBlue ICP-OES (Ametek, Kleve, Germany). Matrix-matched intensity calibration curves were used to quantify total metals, with analytical uncertainties < 5% (as determined by repeat analysis of standards and select samples).

Mössbauer and powder X-ray diffraction (XRD) analysis of mineral phases

^{57}Fe Mössbauer spectroscopy measurements was carried out using a WissEl Elektronik (Germany) instrument that included a close cycle cryostat SHI-850 obtained from Janis Research Company, Inc. (Wilmington, MA), a Sumitomo CKW-21 He compressor unit (Wilmington, MA), and an Ar-Kr proportional counter detector. Sample preparation and operation procedures were identical to previous reports (Zhao et al., 2013). To semi-quantitatively characterize relative amounts of iron phases, Mössbauer spectra were obtained at multiple temperatures: 295 K, 225 K, 77 K, 6 K (Bhattacharyya et al., 2018; Noël et al., 2019). The Mössbauer data were modeled with the Recoil software (University of Ottawa, Canada) using a Voigt-based structural fitting routine (Rancourt and Ping, 1991). XRD characterization of bulk mineralogy was analyzed by a PANalytical X'Pert Multipurpose Diffractometer system with a vertical Q-Q goniometer. The X-ray source was a long-fine-focus, ceramic X-ray tube with a Cu anode, operating at 45 kV and 40 mA. Analysis of the diffraction data (phase matching) was carried out using JADE 9.5.1 (Materials Data, Inc.) and the PDF-4+ database from The International Center for Diffraction Data (v. 2018).

Total C and N, microbial biomass and substrate use efficiency

Total dissolved organic C (DOC) and total dissolved nitrogen (TDN) concentrations were determined for pre- and post-incubation soils as previously described (Weintraub et al., 2007). Briefly, 2 g d.w. soil was extracted with 20 mL of 0.05 M potassium sulfate, agitated for 1 h on an orbital shaker, and filtered through No. 1 Whatman paper. To determine microbial biomass C and N concentrations (MBC and MBN), 2 mL of ethanol-free chloroform were evenly distributed over paired soil subsamples, then incubated at room temperature for 24 h in stoppered 250 mL Erlenmeyer flasks. After fully sparging the chloroform, fumigated samples were extracted as above. We analyzed DOC and TDN concentrations using a Shimadzu TOC-L (Shimadzu Scientific Instruments, Inc. Kyoto, Japan) and calculated MBC and MBN as the difference between paired chloroform-fumigated and non-fumigated subsamples. We lyophilized extracts and measured total C and $\delta^{13}C$ using an elemental analyzer (Carlo Erba NC2500, Lancanshire, UK) coupled to an isotope-ratio mass spectrometer (Finnigan MAT Delta Plus; Thermo Electron Corporation, Bremen, Germany) at the Cornell University Stable Isotope Laboratory. We applied a two-source mixing model (Post, 2002) to assess the relative contribution of native $SO^{12}C$ versus ^{13}C cellulose or glucose to microbial biomass C as follows:

Equation 1 $$f_{sub-C} (\delta_A \delta_C)/(\delta_{sub-C} \delta_C),$$

where f_{sub-C} is the fraction of the C pool derived from ^{13}C-glucose or ^{13}C cellulose; δ_A and δ_C are the $\delta^{13}C$ values of the C pool sampled from substrate-amended and natural abundance (field) soils, respectively; and δ_{sub-C} is the $\delta^{13}C$ of the 99 atom % glucose or cellulose substrate. Microbial substrate use efficiency, estimated as an ecosystem property (SUE_E); (Geyer et al., 2016) was defined by the partitioning of ^{13}C substrate between growth and respiration:

Equation 2 $$SUE_E = {}^{13}MB / ({}^{13}MB + {}^{13}CO_2)$$

where ^{13}MB represents the fraction of ^{13}C-substrate assimilated in microbial biomass (g C g d.w. $soil^{-1}$), and $^{13}CO_2$ represents the fraction of ^{13}C-substrate converted to CO_2 (g C g d.w. $soil^{-1}$) at the end of the incubation period for each substrate and soil. We did not measure the K_{ec} of these soils directly and therefore did not apply a correction factor.

NanoSIMS Method

Bulk soil samples of low_{rain} and $high_{rain}$ were used for microscale analysis. The samples were placed on a Si-wafer and kept at 6 ºC for 1 h. After the cooling period, the Si-wafers were

transferred at room temperature, so that the water condensation attached small soil particles on the wafer surface. The excess of soil was then blown off using an air jet. The samples were then dried in a desiccator at room temperature for subsequent analysis. This approach was chosen instead of the sample dilution in water to avoid displacing the added ^{13}C in the samples. To elucidate the distribution of the mineral particles on the Si-wafer and to choose regions of interests for subsequent NanoSIMS measurements, the samples were assessed by reflected light microscopy (Axio Imager Z2, Zeiss, Oberkochen - Germany) and scanning electron microscopy (SEM) (JSM 5900LV, JEOL, Tokyo - Japan). We have focused the analysis on microaggregates from 10 – 20 µm size.

The samples were imaged using the NanoSIMS 50L instrument (CAMECA, Gennevilliers, France) at the Technical University of Munich. To avoid charging during the NanoSIMS analysis, the samples were coated with an Au/Pd layer of approximately 30 nm (Polaron Emitech SC7640). The Cs^+ primary ion beam was used, with a primary ion impact energy of 16 keV, focused at a spot size of ~150 nm. Prior to the NanoSIMS measurement, contaminants and the Au/Pd coating layer were locally sputtered away using a high primary beam current (pre-sputtering/implantation), while the reactive Cs^+ ions were implanted into the sample, until the secondary ions reached a steady state. In addition to the conductive Au/Pd coating, the internal electron flood gun of the NanoSIMS was used for charging compensation at the measurement time. The primary beam (ca. 2 pA) was scanned over the sample, and $^{12}C^-$, $^{13}C^-$, $^{16}O^-$, $^{12}C^{14}N^-$, $^{27}Al^{16}O^-$, and $^{56}Fe^{16}O^-$ secondary ions were collected on electron multipliers with an electronic dead time fixed at 44 ns. To accurately separate mass isobars (e.g., at mass number 13: $^{13}C^-$ and $^{12}C^1H^-$) the instrument was tuned at high mass resolution. The secondary ions escaping the sample surface, were recorded using a dwell time of 1 ms · $pixel^{-1}$, with 256 × 256 pixels for a 30 × 30 µm field of view with 40 planes per measurement. On average, 1048 μm^2 mineral-dominated and OM-dominated area was imaged for each combination of treatment and substrate with a total of 6286 μm^2 mineral-dominated and OM-dominated area in total. The measurements included 401 microaggregates or particles in total (67 per treatment) with an approximate mean diameter of 5 µm.

For each soil, a control sample containing non-amended field soil was measured to account for instrument stability and instrumental fractionation. For each soil and treatment 4 to 5 areas containing soil particles, previously selected by SEM analyses, were investigated. The NanoSIMS measurements were analyzed using a multi-channel machine-learning segmentation and image

analysis approach as previously described (Schweizer et al., 2018). Briefly, we correct for the electron multiplier dead time with the OpenMIMS plugin for ImageJ (Gormanns et al., 2012). The scanning planes were auto-aligned using the $^{16}O^-$ distribution and sum images of all ion species were computed. To quantify spatial patterns of the soils, two supervised pixel classifications were performed based on the machine-learning algorithm using Ilastik 1.2 (Sommer et al., 2011). This enabled a segmentation including various image features like the intensity, texture and gradient in all isotope distributions. The first segmentation was performed based on the $^{16}O^-$, $^{12}C^- + {}^{13}C^-$ and $^{12}C^{14}N^-$ distributions (Figure S1a). These distributions were used to segment the images into three material classes: background (low counts for all ion species), mineral-dominated (high O−) and dominated by organic matter (OM; high $^{12}C^- + {}^{13}C^-$ and high $^{12}C^{14}N^-$) classes (Figure S1b). The segmentation of the particle surface into mineral-dominated and OM-dominated classes enabled to compare the OM distribution between the samples. A second segmentation based on the $^{13}C^-$: ($^{12}C^- + {}^{13}C^-$) enrichment was performed to account for the high $^{13}C^-$ and low $^{12}C^-$ and $^{12}C^{14}N^-$ segments, derived from the original amended ^{13}C substances (Figure S1c, d). This provides a robust segmentation of the ^{13}C-enriched spots independent of the total $^{12}C^-$ or $^{13}C^-$ counts. By combining the two segmentations, we could differentiate which parts of the mineral-dominated and OM-dominated segments were associated with ^{13}C-enrichment (Fig S1e). This enabled identification of non-enriched, pre-existent, native OM (yielding high counts for C and N species) and the pre-existent OM associated with the amended ^{13}C-enriched substrate (OM-associated ^{13}C-enriched). We compared the area contributions of enriched and native mineral and OM according to their relative proportion of pixels.

Table S1. Summary of NanoSIMS images for each soil condition imaged.

	Low_{rain}			$High_{rain}$		
	Control (unamended)	Glucose-amended	Cellulose-amended	Control (unamended)	Glucose-amended	Cellulose-amended
Particle area (μm^2)	795.5	1027.0	938.4	573.1	2610.4	1846.3
OM-dominated area (μm^2)	75.5	90.9	234.4	228.3	597.6	687.4
^{15}N-enriched area (μm^2)	0.0	27.4	2.1	0.0	51.1	7.9

References

Bhattacharyya, A., Campbell, A.N., Tfaily, M.M., Lin, Y., Kukkadapu, R.K., Silver, W.L., Nico, P.S., Pett-Ridge, J., 2018. Redox Fluctuations Control the Coupled Cycling of Iron and

Carbon in Tropical Forest Soils. Environmental Science and Technology 52, 14129–14139. doi:10.1021/acs.est.8b03408

Chen, C., Kukkadapu, R., Sparks, D.L., 2015. Influence of Coprecipitated Organic Matter on Fe2+(aq)-Catalyzed Transformation of Ferrihydrite: Implications for Carbon Dynamics. Environmental Science and Technology 49, 10927–10936. doi:10.1021/acs.est.5b02448

Eusterhues, K., Wagner, F.E., Häusler, W., Hanzlik, M., Knicker, H., Totsche, K.U., Kögel-Knabner, I., Schwertmann, U., 2008. Characterization of ferrihydrite-soil organic matter coprecipitates by X-ray diffraction and Mössbauer spectroscopy. Environmental Science and Technology 42, 7891–7897. doi:10.1021/es800881w

Geyer, K.M., Kyker-Snowman, E., Grandy, A.S., Frey, S.D., 2016. Microbial carbon use efficiency: accounting for population, community, and ecosystem-scale controls over the fate of metabolized organic matter. Biogeochemistry 127, 173–188. doi:10.1007/s10533-016-0191-y

Gormanns, P., Reckow, S., Poczatek, J.C., Turck, C.W., Lechene, C., 2012. Segmentation of Multi-Isotope Imaging Mass Spectrometry Data for Semi-Automatic Detection of Regions of Interest. PLoS ONE 7. doi:10.1371/journal.pone.0030576

Kanehiro, Y., Whittig, L., 1961. Amorphous Mineral Colloids of Soils of the Pacific Region and Adjacent Areas. Pacific Science 15.

Kukkadapu, R.K., Zachara, J.M., Frederickson, J.K., Smith, S.C., Dohnalkova, A.C., Russell, C.K., 2003. Transformation of 2-line ferrihydrite to 6-line ferrihydrite under oxic and anoxic conditions. American Mineralogist 88, 1903–1914.

Noël, V., Boye, K., Kukkadapu, R.K., Li, Q., Bargar, J.R., 2019. Uranium storage mechanisms in wet-dry redox cycled sediments. Water Research 152, 251–263. doi:10.1016/j.watres.2018.12.040

Noor, N., Thompson, A., 2022. Localized alteration of ferrihydrite natural organic matter coprecipitates following reaction with Fe(II). Soil Science Society of America Journal 1–11. doi:10.1002/saj2.20366

Post, D.M., 2002. Using stable isotopes to estimate trophic position: Models, methods, and assumptions. Ecology 83, 703–718. doi:10.1890/0012-9658(2002)083[0703:USITET]2.0.CO;2

Rancourt, D.G., Ping, J.Y., 1991. Voigt-based distributions methods for arbitrary-shape in Miissbauer spectroscopy static hyperfine parameter. Nuclear Instruments and Methods in Physics Research Section B: Beam Interactions with Materials and Atoms 58, 85–97.

Schweizer, S.A., Hoeschen, C., Schlüter, S., Kögel-Knabner, I., Mueller, C.W., 2018. Rapid soil formation after glacial retreat shaped by spatial patterns of organic matter accrual in microaggregates. Global Change Biology 24, 1637–1650. doi:10.1111/gcb.14014

Sommer, C., Straehle, C., Ullrich, K., Hamprecht, F.A., 2011. Ilastik : Interactive learning and segmentation toolkit ilastik : Interactive Learning and Segmentation Toolkit. doi:10.1109/ISBI.2011.5872394

Weintraub, M.N., Scott-Denton, L.E., Schmidt, S.K., Monson, R.K., 2007. The effects of tree rhizodeposition on soil exoenzyme activity , dissolved organic carbon , and nutrient availability in a subalpine forest ecosystem. Oecologia 154, 327–338. doi:10.1007/s00442-007-0804-1

Zhao, L., Dong, H., Kukkadapu, R., Agrawal, A., Liu, D., Zhang, J., Edelmann, R.E., 2013. Biological oxidation of Fe (II) in reduced nontronite coupled with nitrate reduction by *Pseudogulbenkiania* sp. Strain 2002. Geochimica et Cosmochimica Acta 119, 231–247. doi:10.1016/j.gca.2013.05.033

Figure S1. Multichannel image analysis of NanoSIMS measurements based on a machine-learning algorithm. The first segmentation was done based on the $^{16}O^-$, $^{12}C^- + {}^{13}C^-$ and $^{12}C^{14}N^-$ distributions (a) which enabled the classification of mineral-dominated and OM-dominated areas (b). For a second segmentation we used the $(^{12}C^- + {}^{13}C^-):{}^{13}C^-$ enrichment ratio (c) to identify ^{13}C-enriched and non-enriched, native areas independent of the first segmentation (d). By combining the two segmentations, we could quantify mineral-associated and OM-associated ^{13}C-enriched areas and compare them with non-enriched areas (e).

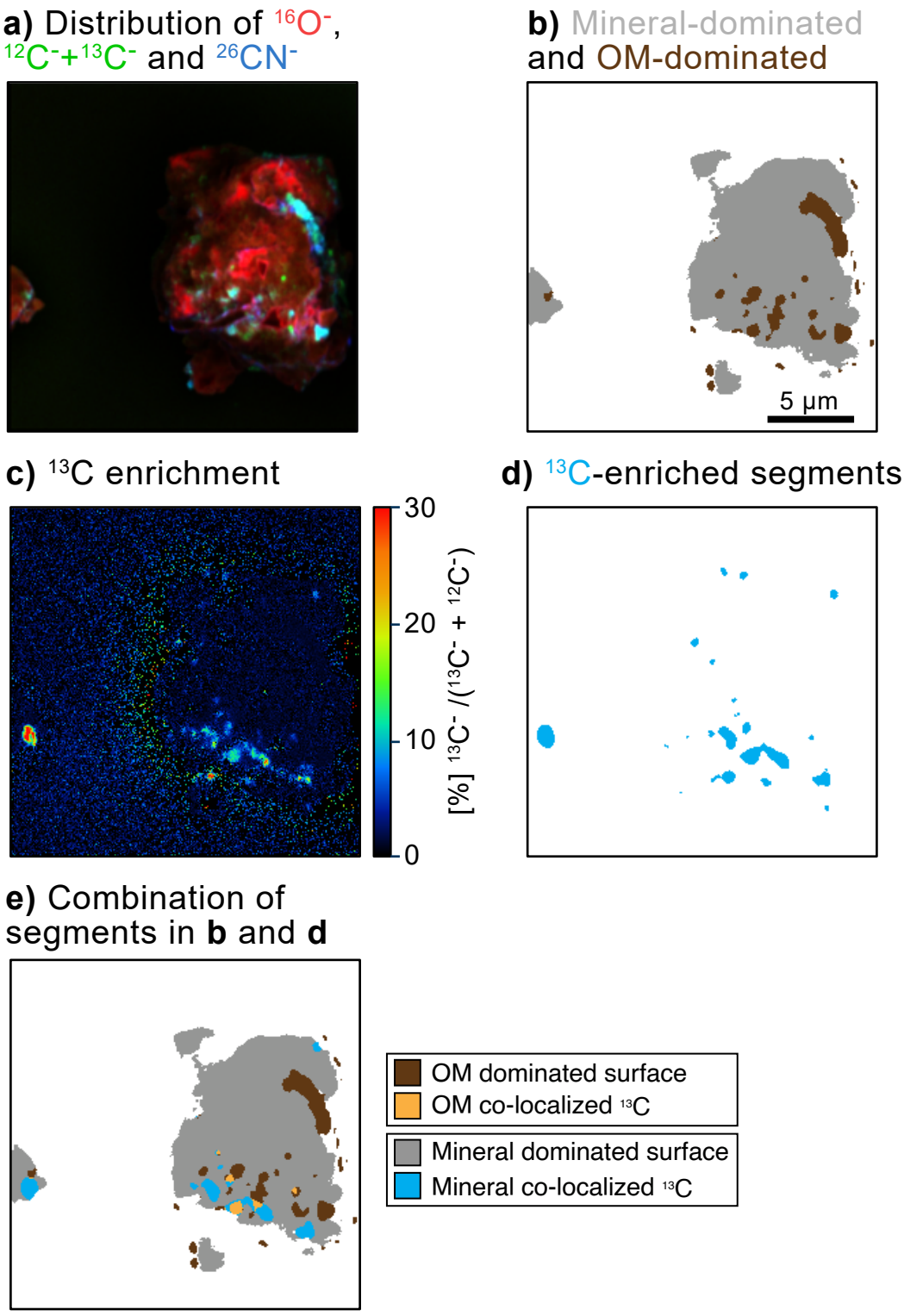

Figure S2. Powder XRD spectra for (A) $high_{rain}$ (B) and low_{rain} soils. The extent of poorly crystalline / amorphous material is evident in the high number of features between 20-70 2θ (Cu Kα).

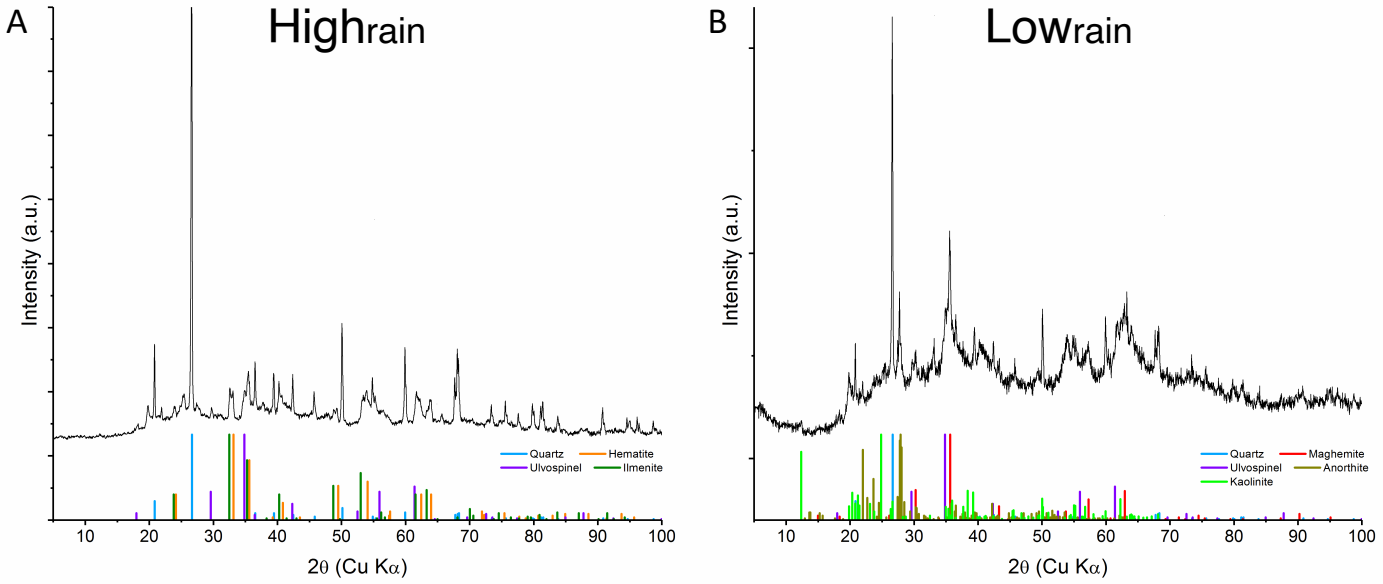

Figure S3. Experimental and modeled Mössbauer spectra of $high_{rain}$ and low_{rain} soils at RT, 225 K, 77 K, and 6 K. In (a), spectra were obtained at various temperatures to identify and characterize relative amounts of various phases of iron minerals. In (b), modeled Gaussian magnetic hyperfine filed distributions of the ferrihydrite-OM complexes (Ferr-OM-1 and Ferr-OM-2) reveals a shift that indicates lower C:Fe in the $high_{rain}$ relative to low_{rain} soils.

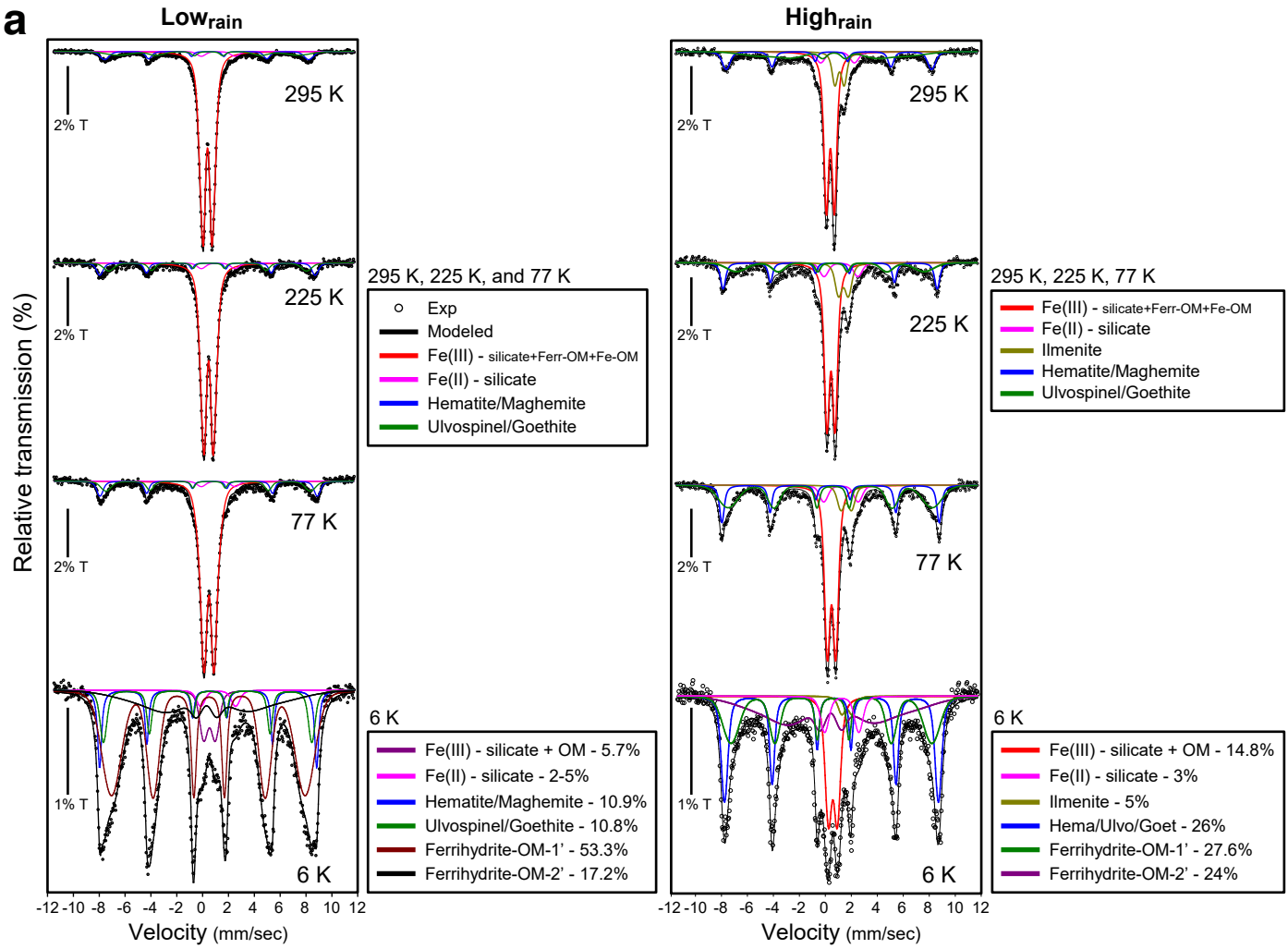

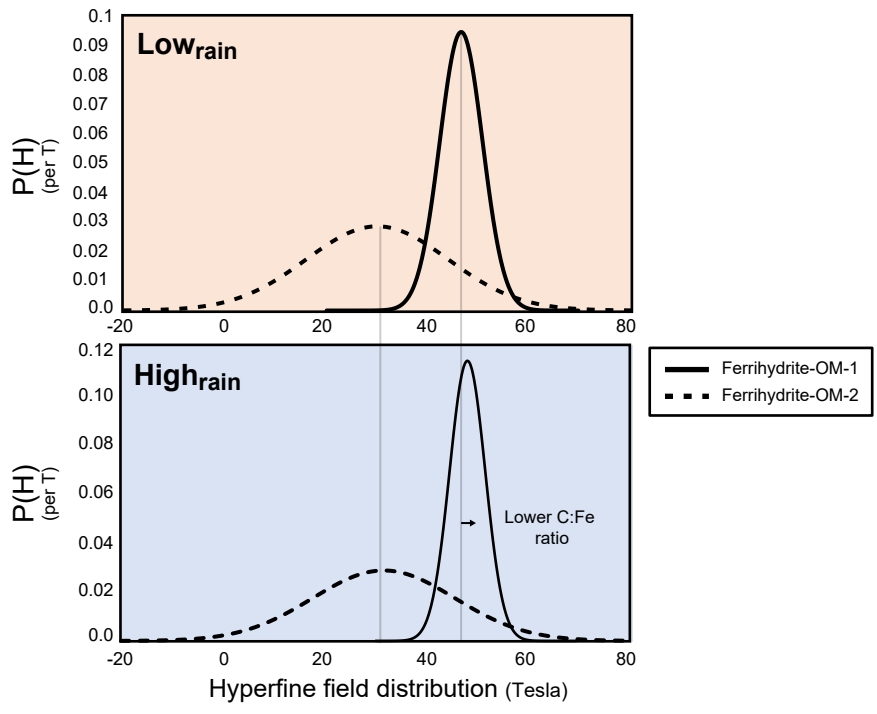

Figure S4. Total dissolved organic carbon in the KCl and hydroxylamine hydrochloride (HH) extracts for each soil and substrate type. Extraction blanks are also included. Significant differences between soil type, without distinction for extraction method or substrate, were tested using the Wilcoxon test (*; $p \leq 0.05$, **; $p \leq 0.01$).